

## Optimization of submerged floating tunnel cross section based on parametric Bézier curves and hybrid backpropagation - genetic algorithm

Zou, Pengxu; Bricker, Jeremy; Uijtewaal, Wim

**DOI**

[10.1016/j.marstruc.2020.102807](https://doi.org/10.1016/j.marstruc.2020.102807)

**Publication date**

2020

**Document Version**

Final published version

**Published in**

Marine Structures

**Citation (APA)**

Zou, P., Bricker, J., & Uijtewaal, W. (2020). Optimization of submerged floating tunnel cross section based on parametric Bézier curves and hybrid backpropagation - genetic algorithm. *Marine Structures*, 74, Article 102807. <https://doi.org/10.1016/j.marstruc.2020.102807>

**Important note**

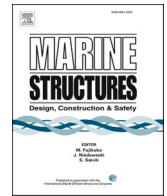
To cite this publication, please use the final published version (if applicable). Please check the document version above.

**Copyright**

Other than for strictly personal use, it is not permitted to download, forward or distribute the text or part of it, without the consent of the author(s) and/or copyright holder(s), unless the work is under an open content license such as Creative Commons.

**Takedown policy**

Please contact us and provide details if you believe this document breaches copyrights. We will remove access to the work immediately and investigate your claim.



# Optimization of submerged floating tunnel cross section based on parametric Bézier curves and hybrid backpropagation - genetic algorithm

Pengxu Zou<sup>a,b,c,\*</sup>, Jeremy Bricker<sup>a</sup>, Wim Uijtewaal<sup>a</sup>

<sup>a</sup> Department of Hydraulic Engineering, Delft University of Technology, Delft, the Netherlands

<sup>b</sup> CCCC FHDI Engineering Co., Ltd., Guangzhou, China

<sup>c</sup> CCCC SFT Technical Joint Research Team, Zhuhai, China

## ARTICLE INFO

### Keywords:

Submerged floating tunnel  
Cross-section optimization  
Hybrid BP-GA  
CFD

## ABSTRACT

The cross-section geometry of a submerged floating tunnel (SFT) has a large effect on hydrodynamic characteristics, structural behavior and service level, making the tunnel cross section the primary factor in optimizing efficiency. Minimizing the mean drag and the dynamic variability in the lift of the SFT cross section under bi-directional (i.e., tidal) flow has a dramatic impact on the reduction of structural displacements and mooring loads. Based on a parametric Bézier curve dynamically comprising the leading-edge radius, tunnel height and width to define the SFT geometry, a sensitivity analysis of the Bézier curve parameters for a fixed aspect ratio with prototype dimensions under uniform flow conditions was conducted by applying Computational Fluid Dynamics (CFD), and the pressure distribution around the SFT cross-section surface was analyzed. A theoretical method comprising the Kármán vortex street parameters was employed to verify the CFD simulation results. In order to determine the SFT cross section with optimal hydrodynamic properties, the mean drag and Root Mean Square (RMS) lift coefficients were selected as optimization objectives, and four Bézier curve parameters were the input variables, in a neural network and genetic algorithm optimization process (a hybrid BP-GA structure), which is less likely to become trapped in local minima. The results show the optimal tunnel cross section has a mean drag and a RMS lift coefficient reduced by 0.9% and 6.3%, respectively, compared to the original CFD dataset.

## 1. Introduction

The submerged floating tunnel (SFT), also called “Archimedes Bridge”, is a new type of sea crossing that takes advantage of buoyancy to support its weight, and a mooring system to balance the residual buoyancy and limit the displacement of the SFT tube [1, 2]. Since the concept was brought forward, research is still limited to theoretical and small-scale experimental verification, and no prototype has yet been built [3].

The cross-section geometry of the SFT has a large effect on hydrodynamic characteristics, space utilization, structural behavior, service level and construction cost, making the geometry a primary factor in optimizing efficiency and thus a priority to be optimized at the feasibility analysis stage of design. Moreover, due to the possibility of bidirectional ambient flow incident on both leading and

\* Corresponding author. Department of Hydraulic Engineering, Delft University of Technology, Delft, the Netherlands.  
E-mail address: [p.zou@tudelft.nl](mailto:p.zou@tudelft.nl) (P. Zou).

<https://doi.org/10.1016/j.marstruc.2020.102807>

Received 3 January 2020; Received in revised form 30 April 2020; Accepted 23 June 2020

Available online 24 July 2020

0951-8339/© 2020 The Authors. Published by Elsevier Ltd. This is an open access article under the CC BY-NC-ND license

(<http://creativecommons.org/licenses/by-nc-nd/4.0/>).

trailing edges, potential flow theory and the Kutta condition [4] applied in traditional airfoil optimization design cannot be used due to flow separation from the bluff body, which makes the flow field complex.

Li et al. [5] conducted an experiment to compare the pressure characteristics of SFT's with circular, elliptical and polygonal sections under wave impacts, and concluded that the circular section experiences the largest wave forces. Li and Jiang [3] conducted numerical simulations to compare the pressure distributions of two cross sections by combining fluid mechanical calculation and structural analysis, concluding that an elliptical section experiences smaller displacements and stress than a rectangular section. Gang et al. [6] compared rectangular, circular, and elliptical floating tunnel cross-section forms, and determined the response to an explosion shock wave by using the finite element software LS-DYNA [7]. Since research about SFT cross sections is scarce, geometrical optimization and applications from other engineering fields such as aerospace and mechanical engineering are helpful. Hajabdollahi et al. [8] used a Non-dominated Sorting Genetic Algorithm-II (NSGA-II) to maximize heat transfer rate and fin efficiency for a fin geometry optimization. Basumatary et al. [9] modified and optimized a conventional two-bladed Savonius water turbine section by considering design parameters including gap width and overlap ratio, using CFD solvers to develop a new, combined lift-drag based blade design method. Wang et al. [10] presented a new cross section based on a meridian surface optimization strategy with the integration of Medial Axis Transform (MAT) design theory, CFD analysis, Central Composite Design (CCD), Response Surface Method (RSM) and NSGA-II. Lee et al. [11] employed the equivalent static load method for non-linear static response structural optimization (ESLSO) to determine workpiece shape in the forging process. Garg et al. [12] used a high-fidelity hydrostructural solver combined with a gradient-based optimizer to conduct numerical predictions compared with experimental measurements for a baseline NACA 0009 hydrofoil and an optimized hydrofoil.

Based on SFT cross-section analysis to date, the elliptical cross section has good hydrodynamic characteristics due to its streamlined shape compared with a square bluff shape [3]. Though many simple sections including circle, ellipse, polygon, and square have been assessed as SFT cross sections, there is still a need to conduct a detailed parametric study to determine an optimal shape. This paper is structured as follows. In section 2, a SFT cross-section profile with various geometries was determined by a parametric Bézier curve [13,14]. Section 3 validated the CFD model against a laboratory experiment and theory. The main hydrodynamic characteristics including drag ( $C_d$ ) and lift coefficients ( $C_l$ ) were obtained by the ANSYS Fluent version 19.1 CFD solver [15] applied in a high-performance computing (HPC) cluster to run parallel computation tasks. The dependence of average  $C_d$  and  $C_l$  magnitude on the Bézier curve parameters was presented in section 4. Section 5 applied a neural network (NN) optimized by genetic algorithm (GA) to relate tunnel cross-section parameters with optimal hydrodynamic properties, and further verified this by numerical simulations.

## 2. Parametric design of tunnel cross-section

### 2.1. Parametric Bézier curve

The Bézier-PARSEC (BP) curve method is one of the most common parametric design methods for airfoils, because it tends to minimize the drag force of the geometry. The BP curve is developed to extend and improve the typical Bezier parameterization, which has been applied frequently in airfoil design [16,17]. The BP curve combines the advantages of both Bézier variables and PARSEC parameters, to reduce the nonlinear interaction among parameters, making the parameters directly link to the objective function, and avoiding the second-order discontinuity problem. Bézier curves have a limited number of degrees of freedom determined by their control points and improve the convergence rate for aerodynamic optimization using Differential Evolution [18]. Moreover, it is desirable to determine parameters such as the leading-edge radius and tunnel height, which affect lift and drag, by using the PARSEC parameters [19]. As the BP curve method sees widespread use in airfoil design, it is the first method we use to define the SFT cross-section geometry.

In this study, however, due to the possibility of bi-directional (i.e., tidal) flow, the leading and trailing halves of the SFT cross section were designed to be symmetric. To describe the tunnel geometry, four control points in each quadrant were considered as variables. These parametric Bézier curve and control points are shown in Fig. 1(a).

Third-degree parametric Bézier curves were used for the definition of the SFT cross-section profile. These are given by

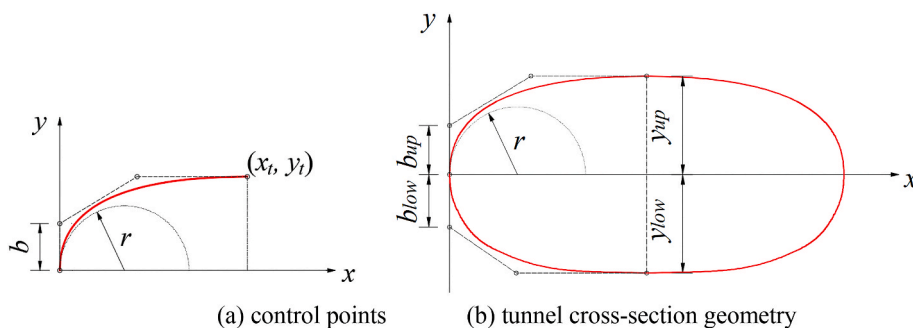


Fig. 1. Third-degree Bézier curve.

$$\begin{aligned} x(u) &= x_0(1-u)^3 + 3x_1u(1-u)^2 + 3x_2u^2(1-u) + x_3u^3 \\ y(u) &= y_0(1-u)^3 + 3y_1u(1-u)^2 + 3y_2u^2(1-u) + y_3u^3 \end{aligned} \tag{1}$$

where  $u$  is a variable with a range of 0–1.

The four control points that determine the shape of one quadrant of the SFT cross section are given by

$$\begin{aligned} x_0 &= 0 & y_0 &= 0 \\ x_1 &= 0 & y_1 &= b \\ x_2 &= 3b^2/2r & y_2 &= y_t \\ x_3 &= x_t & y_3 &= y_t \end{aligned} \tag{2}$$

where  $b$  is subject to the following restriction

$$0 < b < \min\left(y_t, \sqrt{2rx_t/3}\right)$$

Since Bezier parameters are standard in airfoil design, a detailed derivation of these parameters and constraint conditions can be found in Rogalsky [19].

### 2.2. Dimension limitation

Referring to the current feasibility study and possible considerations of the traffic volume for the SFT cross section [20–22], two 3.5 m wide lanes and a curb or sidewalk of width  $R$  on either side should be considered to meet the requirement for a typical two-lane tunnel (Fig. 2). Based on the guidelines of AASHTO [23], the total clearance between walls should be a minimum of 9 m, and the vertical clearance  $H$  should be a minimum of 4.3 m or 4.9 m. According to JTG/T D70 [24], the minimum width clearance  $W$  should be 7.5–11 m with different vehicle design speeds requirements, and the minimum vertical clearance  $H$  should be 4.5 m or 5 m depending on the highway classification.

SFT cross section dimensions  $H = 5$  m and  $W = 10$  m, with an aspect ratio  $H/W = 0.5$ , were chosen for analysis in this study. Since here we focus mainly on the cross-section shape, it should be noted that in the actual tunnel cross section design, requirements for minimum lateral and vertical clearance must also be met. Each quadrant of parametric Bézier curves was defined by 4 control points. To freeze the aspect ratio of the tunnel cross section, the locations of the leading edge and trailing edge, and the height of the tunnel, were kept fixed. Therefore, the parameter constraints of the four control points (Fig. 1(a)) are given by

$$\begin{aligned} 0 &< r \leq 2.5 \\ x_t &= 5 \\ 0 &\leq y_t \leq 5 \end{aligned}$$

The junction between the upper and lower curves at the leading edge should have the same leading-edge radius to avoid divergence of calculation. Due to the fixed length and height of the cross section (aspect ratio = 0.5),  $y_{low}$  can be determined by  $H - y_{up}$  (Fig. 1(b)). As the tunnel profile is comprised of the upper and lower halves and the symmetrical shape of leading and trailing halves, the remaining variables are:  $y_{up}$ ,  $r$ ,  $b_{up}$  and  $b_{low}$ .

## 3. Modeling validation

### 3.1. Grid Independent Limit test

Two-dimensional (2D) SFT cross sections with various geometrical parameters were designed with computer-aided design (CAD) tools and the ANSYS Design Modeler. The mesh of the CFD computation domain was generated by ANSYS Mesh. A Grid Independent Limit (GIL) test was carried out to ensure the mesh convergence and validation of computational results by refining element size until

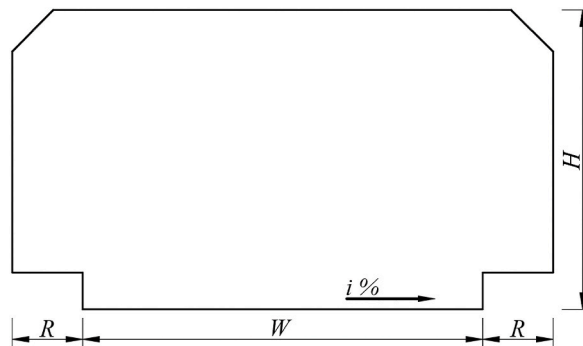


Fig. 2. Typical two-lane tunnel cross section,  $i$  = slope.

an optimum mesh quality and stable results were achieved. To evaluate the quality of the mesh, a GIL was conducted by continuously changing the domain maximum element size and the SFT surface element size, and comparing the wall  $Y^+$ , statistical values of  $C_d$  and  $C_l$  around the SFT cross-section surface. A triangular mesh was used as is widely applicable for curved and complex geometries.

Table 1 shows the GIL test result for the SFT cross-section profile with parameters  $b_{up} = b_{low} = 1$  m,  $r = 4$  m,  $y_{up} = 2.5$  m under a uniform cross-flow velocity of 0.1 m/s. It shows that the wall  $Y^+$  of all the cases are below 300, which is within the acceptable range [25], and it signifies the standard wall function condition and the quality of the minimum mesh size are sufficient. The maximum element size (1 m or 0.5 m) seems to have almost no influence on  $C_d$  or  $C_l$ , proving that numerical stability and mesh size convergence are achieved (Fig. 3). Hence the maximum element size 1 m and the minimum element size 0.01 m are chosen for all analyzed cases, with a minimum orthogonality of 0.41 after mesh improvement.

As the unsteady Reynolds-averaged Navier-Stokes (URANS) calculation has a good accuracy compared with steady RANS [26], URANS was applied in this study. The Pressure-Implicit with Splitting of Operators (PISO) algorithm was applied for pressure-velocity coupling as it maintains a stable calculation with a larger time step with neighbor correction, and it is highly recommended in transient simulations compared with SIMPLE and SIMPLC [27–29]. The boundary condition at the sides and cylinder wall was a rough wall layer approximation. The “velocity-inlet” and the “outlet” boundary conditions were employed at the inlet and exit boundaries, respectively. The inlet boundary had a turbulence intensity of 2.8% with a turbulent length scale of 10 m. The wall roughness of the tunnel surface was 3 mm [30], based on actual concrete. The inlet and upper/lower boundaries were set 5W away from the cylinder axis, and the outlet was set 15W away from the cylinder. The maximum CFL number was 0.5, and the non-dimensional time step  $\delta t U/W$  was kept at  $4 \times 10^{-4}$ . The simulation domain is shown in Fig. 4.

### 3.2. Turbulence modeling

The  $k-\epsilon$  turbulence model generally produces accurate results in high Reynolds number conditions [31,32]. The RNG  $k-\epsilon$  model gives more accurate simulations for dramatically irregular geometry with flow separation via an additional term in its  $\epsilon$  equation. Also, an analytical formula for the turbulent Prandtl number is provided, in contrast to the constant value used in the standard  $k-\epsilon$  model. These features make the RNG  $k-\epsilon$  model more accurate and reliable than the standard  $k-\epsilon$  model for a wider range of flows. The RNG  $k-\epsilon$  model transport equation can be expressed as Eq. (3).

$$\begin{aligned} \frac{\partial}{\partial t}(\rho k) + \frac{\partial}{\partial x_i}(\rho k u_i) &= \frac{\partial}{\partial x_j} \left( \alpha_k \mu_{eff} \frac{\partial k}{\partial x_j} \right) + G_k + G_b - \rho \epsilon - Y_M + S_k \\ \frac{\partial}{\partial t}(\rho \epsilon) + \frac{\partial}{\partial x_i}(\rho \epsilon u_i) &= \frac{\partial}{\partial x_j} \left( \alpha_\epsilon \mu_{eff} \frac{\partial \epsilon}{\partial x_j} \right) + C_{1\epsilon} \frac{\epsilon}{k} (G_k + C_{3\epsilon} G_b) - C_{2\epsilon} \rho \frac{\epsilon^2}{k} + G_b - R_\epsilon + S_\epsilon \end{aligned} \tag{3}$$

The additional term in the  $\epsilon$  equation is given by Eq. (4)

$$R_\epsilon = \frac{C_\mu \rho \eta^3 (1 - \eta/\eta_0) \epsilon^2}{1 + \beta \eta^3} \frac{\epsilon^2}{k} \tag{4}$$

where  $\eta \equiv S_k/\epsilon$ ,  $\eta_0 = 4.38$ ,  $\beta = 0.012$ .

The turbulent viscosity is computed by combining  $k$  and  $\epsilon$  as follows in Eq. (5)

$$\mu_t = \rho C_\mu \frac{k^2}{\epsilon} \tag{5}$$

where  $C_{1\epsilon} = 1.42$ ,  $C_{2\epsilon} = 1.68$ , and  $C_\mu = 0.085$  are all dimensionless user-adjustable parameters derived using the RNG theory. Hence, a numerical model integrating the two-dimensional, incompressible flow, unsteady RNG  $k-\epsilon$  turbulence model with the standard wall function was adopted.

### 3.3. Numerical verification

As one of the canonical and classical problems in fluid mechanics, the cylinder-flow case is of great interest and importance for a wide range of offshore engineering applications, including marine pipelines, offshore platform support legs, and thus also the SFT. Considering the prototype scale of the SFT cross section and current conditions in deep sea, the Reynolds number can be higher than  $1 \times 10^6$ , which encompasses both supercritical ( $4-5 \times 10^5$  and  $2.5-4 \times 10^6$ ) and transcritical ( $>2.5-4 \times 10^6$ ) flow régimes [33]. To date, both experimental tests and numerical simulations of circular cylinders at very high Reynolds number flows ( $Re > 10^7$ ) are lacking due

**Table 1**  
Mesh size for the GIL test.

| $S_{max}$ (m) | $S_{min}$ (m) | $N_{Cells}$ | $Y^+$   | $C_{d,m}$ | $C_{l,rms}$ |
|---------------|---------------|-------------|---------|-----------|-------------|
| 2             | 0.03          | 27,572      | 120–180 | 0.116     | 0.102       |
| 2             | 0.01          | 54,416      | 40–70   | 0.140     | 0.153       |
| 1             | 0.01          | 137,990     | 40–70   | 0.142     | 0.156       |
| 0.5           | 0.01          | 376,768     | 40–70   | 0.143     | 0.157       |

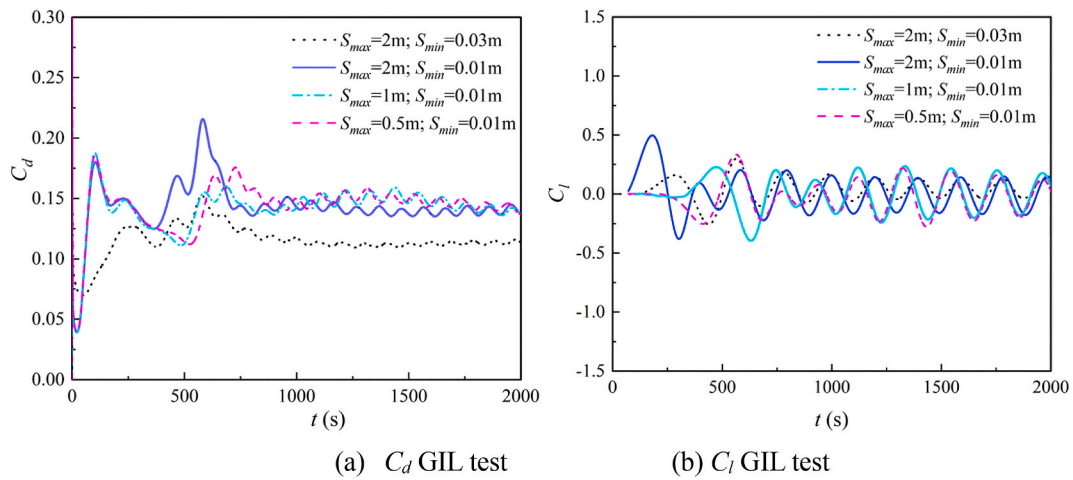


Fig. 3. GIL test results.

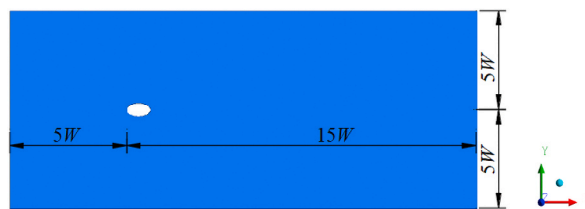


Fig. 4. Schematic diagram of the computational domain.

to the complexity of the flow characteristics and limitations of laboratory equipment. Herein  $Re = 1 \times 10^6$  was chosen for validation and simulation in the optimal cross section analysis, because sufficient experimental data is available.

To evaluate the model's validity under very high Reynolds numbers, simulated average drag and pressure coefficients were compared with published experimental results by James et al. [33]. A cylinder within a rectangular domain was used under the same Reynolds number and relative surface roughness (the ratio of surface roughness to model diameter). The Reynolds number (expressed as Eq. (6)), based on the upstream flow speed  $U = 0.1$  m/s and a cylinder diameter of 10 m, has a magnitude of  $1 \times 10^6$ .

$$Re = \frac{\rho U d}{\mu} \tag{6}$$

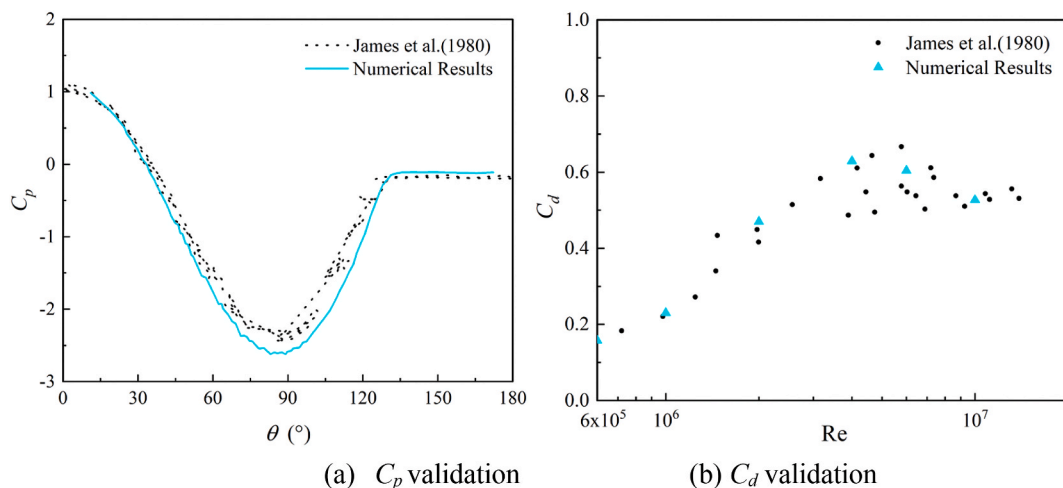


Fig. 5. Verification of numerical results against the laboratory experiments of James et al. (1980).

where  $d$  is the characteristic length, which is diameter of the cylinder or chord length applied in airfoil design. Hereinafter the clearance width  $W$  was used for the SFT cross-section analysis.

The mean pressure coefficient  $C_p$  (expressed as Eq. (7)) distribution around the cylinder compared with the experimental data measured in the counterclockwise direction is shown in Fig. 5 (a).

$$C_p = \frac{p - p_{ref}}{\frac{1}{2}\rho U^2} \tag{7}$$

where  $p$  is the pressure on the cylinder, and  $p_{ref}$  is the reference pressure.

It is noted that the mean  $C_p$  curves of both the physical model test and numerical result show the separation point occurring approximately  $120^\circ$  aft of the forward stagnation point, which is a typical characteristic of the supercritical flow régime, indicating the presence of separation in the wake region. A narrower wake can exist caused by boundary layer transition, reattachment and backward turbulent separation; this is associated with lower drag and is commonly known as the drag crisis.

Fig. 5 (b) shows the results for validation concerning the drag coefficient. In order to verify the drag coefficient distribution clearly in the drag crisis region,  $Re = 6 \times 10^5, 2 \times 10^6, 4 \times 10^6, 6 \times 10^6, 1 \times 10^7$  were also added for the validation. The experimental data and numerical results follow the same trend with reasonable agreement.

In order to validate simulated lift, CFD results were compared with a theoretical method derived by Sallet [34], which comprises expressions for the fluctuating lift coefficient of any bluff cylindrical body as a function of Kármán vortex street parameters [34]:  $S_t, l$  and  $h$  by employing potential flow theory. The equations for  $C_d$  and  $C_l$  are shown as Eqs. (8) and (9), assuming von Kármán’s stability criterion of vortex spacing ratio  $\frac{h}{l} = 0.280549$ .

$$S_t^2 \left(\frac{l}{W}\right)^3 + 0.529 \left(\frac{l}{W}\right)^2 - 1.529 \frac{l}{W} + 1.593 C_d = 0 \tag{8}$$

$$C_l = \sqrt{2} \frac{l}{W} \left(1 - \frac{S_t l}{W}\right) \left(3 \frac{S_t l}{W} - 2\right) \tag{9}$$

The inversely proportional relationship between  $C_d$  and  $S_t$  is clear from Eq. (8). Based on the theory, for given numerical results of  $C_d$  and  $S_t$ ,  $l$  can be calculated in terms of  $W$  by means of Eq. (8), and then  $C_l$  can be determined by employing Eq. (9). Therefore, numerical simulation results for  $l$  and  $C_l$  can be validated by this theoretical method within the supercritical Reynolds number range.

The SFT cross section used for this validation test was determined by the parametric Bézier curve with  $b_{up} = b_{low} = 0.5$  m,  $y_{up} = 2.5$  m, and  $r = 0.1$  m,  $0.5$  m,  $1.0$  m,  $1.5$  m,  $2.5$  m,  $4.5$  m. The comparison of numerical and theoretical results are shown in Table 2, which shows a close agreement in  $C_l$  for bluff bodies (larger  $r$ ). Flow visualization supported by CFD makes observation of von Kármán vortices feasible, and important phenomena like the vortex street parameters and the occurrence of stagnation can be clearly evaluated. The fluctuation of  $C_l$  hence can be correctly predicted by applying the vortex street model.

Both  $l$  and  $C_l$  follow the same trend as  $C_d$  and  $S_t$  change, and numerical and theoretical  $C_l$  values are fairly close when  $r > 0.5$  m. The maximum relative  $C_l$  difference of 40.8% and the deviation of  $l$  can be explained by the limitations of the theoretical method, which is based on idealizing the vortex wake as two parallel rows of vortices, and neglecting the tunnel surface roughness and viscous contribution to the drag force. Despite its basic limitations, the theoretical method can at least reveal the effect of the SFT cross section profile on vortex street parameters and allow verification of the CFD lift coefficient in a Reynolds number range where experimental data are not available.

## 4. Model analysis and discussion

### 4.1. Performance metrics

For hydrodynamic characteristics of a SFT cross section design, the essential parameters are drag and lift coefficients. Due to the uncertainty of current velocity and direction, the lift or drag force of the tunnel cross section exerted by a current can vary substantially, possibly causing excessive loading or fatigue damage to the mooring system, and also difficulty of operation due to the need for regulating ballast water to balance the variable lift force. Hence, the optimization objectives are to decrease the fluctuation

**Table 2**  
Comparison between numerical and theoretical lift coefficients.

| R (m) | $C_d$ | $S_t$ | $l$ (m)            |                  | $C_l$              |                  | Relative difference |
|-------|-------|-------|--------------------|------------------|--------------------|------------------|---------------------|
|       |       |       | Theoretical result | Numerical result | Theoretical result | Numerical result |                     |
| 0.1   | 0.234 | 0.213 | 22.73              | 12.55            | 0.191              | 0.322            | 40.8%               |
| 0.5   | 0.156 | 0.216 | 22.64              | 12.00            | 0.131              | 0.149            | 11.8%               |
| 1.0   | 0.151 | 0.221 | 22.11              | 11.98            | 0.130              | 0.139            | 6.1%                |
| 1.5   | 0.151 | 0.222 | 22.01              | 11.97            | 0.130              | 0.137            | 5.1%                |
| 2.5   | 0.150 | 0.223 | 21.91              | 11.63            | 0.131              | 0.129            | 1.6%                |
| 4.5   | 0.154 | 0.220 | 22.20              | 11.94            | 0.131              | 0.131            | 0.0%                |

amplitude of lift and drag forces. Both the drag and lift forces can be expressed with non-dimensional force coefficients,  $C_d$  and  $C_l$ , given in Eq. (10).

$$C_{l,d} = \frac{F_{l,d}}{\frac{1}{2}\rho U^2 W} \tag{10}$$

where  $F_{l,d}$  is the lift or drag force per unit meter.

Since the fluctuation amplitude of  $C_d$  is small compared with  $C_l$ , and the fluctuation amplitude variation of  $C_l$  acts as a fatigue load on the mooring system, the variability of  $C_l$  is represented by its RMS  $C_{l,rms}$ , which represents how much the lift coefficient is oscillating [35]. The RMS is given by Eq. (11)

$$x_{rms} = \sqrt{\frac{\sum_{i=1}^n x_i^2}{n}} \tag{11}$$

where  $x_i$  is a variable comprising a time series of data. For  $C_d$  and  $S_b$ , the mean value is much larger than the fluctuation, so the mean (not the RMS) was calculated. To obtain reliable statistics and allow model spin-up time, an unsteady simulation of 4000 non-dimensional time steps was performed and the last 600 time steps were used.  $S_t$  was calculated from adjacent peaks of the lift coefficient time series. The objective of the SFT cross-section shape optimization is to minimize  $C_{l,rms}$  and  $C_{d,m}$ .

#### 4.2. Effects of $y$

Fig. 6 shows  $C_{l,rms}$ ,  $S_{t,m}$  and  $C_{d,m}$  for the cases  $b_{low} = b_{up} = 1$  m,  $r = 2.5$  m and  $y_{up} = 3.5$  m, 3 m, 2.5 m, 2 m, 1.5 m. The velocity magnitude contours of the three cases are shown in Fig. 7. As the total height of the SFT cross section is 5 m, decreasing  $y_{up}$  means increasing  $y_{low}$ ; thus  $y_{up} = 2.5$  m produces symmetry in the upper and lower halves of the cross section. When  $y_{up} = 2.5$  m, half of the total tunnel height,  $C_{l,rms}$  and  $C_{d,m}$  take their minimum values, and  $S_{t,m}$  takes its maximum value. When  $y_{up} > 2.5$  m, both  $C_{l,rms}$  and  $C_{d,m}$  increase. The mechanism underlying this increase of  $C_d$  and  $C_l$  due to increased  $y_{up}$  can be interpreted as follows: as the flow passes around the leading edge of the tunnel profile, the flow streamline is distorted by the bluff shape, which causes an increase in the velocity gradient. The velocity gradient is related to the profile curvature. The curvature of the upper half increases with increasing  $y_{up}$ , and thus generates a more cambered upper half and flatter lower half, hence increasing the velocity magnitude (Fig. 7) and decreasing the pressure around the cross section upper half based on Bernoulli's principle. The lower half shows the opposite tendency, causing an increasing in the overall  $C_l$  of the cross section. The large curvature of the upper half also causes the boundary layer separation point to move upstream, so the width of the wake region increases, which leads to an increase of  $C_d$  and  $C_b$ , and a decrease of  $S_t$ . This behavior agrees with experimental results which compare aerodynamic properties of a flat thin plate with a cambered plate in a water tunnel [36].

#### 4.3. Effect of $r$

Fig. 8 shows  $C_{l,rms}$ ,  $S_{t,m}$  and  $C_{d,m}$ , and Fig. 9 shows the pressure coefficient along both upper and lower halves of the SFT cross section when lift reaches its peak value for  $b_{up} = b_{low} = 0.5$  m,  $y_{up} = 2.5$  m, and  $r = 0.1$  m, 0.5 m, 1.0 m, 1.5 m, 2.5 m, 4.5 m.

It can be seen that with increasing  $r$ ,  $C_{d,m}$  and  $C_{l,rms}$  decrease remarkably and then increase slightly, with a minimum value around  $r = 2.5$  m, while  $S_{t,m}$  shows an inverse relationship. For  $r = 0.1$  m with a fixed aspect ratio, the sharp leading edge and apex shape are obtained due to the extremely small radius, which causes a complete flow separation from the apex and nadir points (Fig. 10(a)). At small  $r$ , the width of the wake region is large. As a result, lower pressure and a wider wake recirculation region occur near the trailing

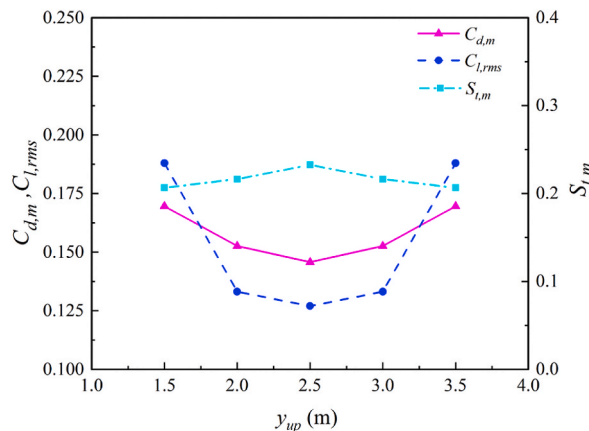


Fig. 6. Variation of dimensionless lift, drag, and Strouhal number with  $y_{up}$ .

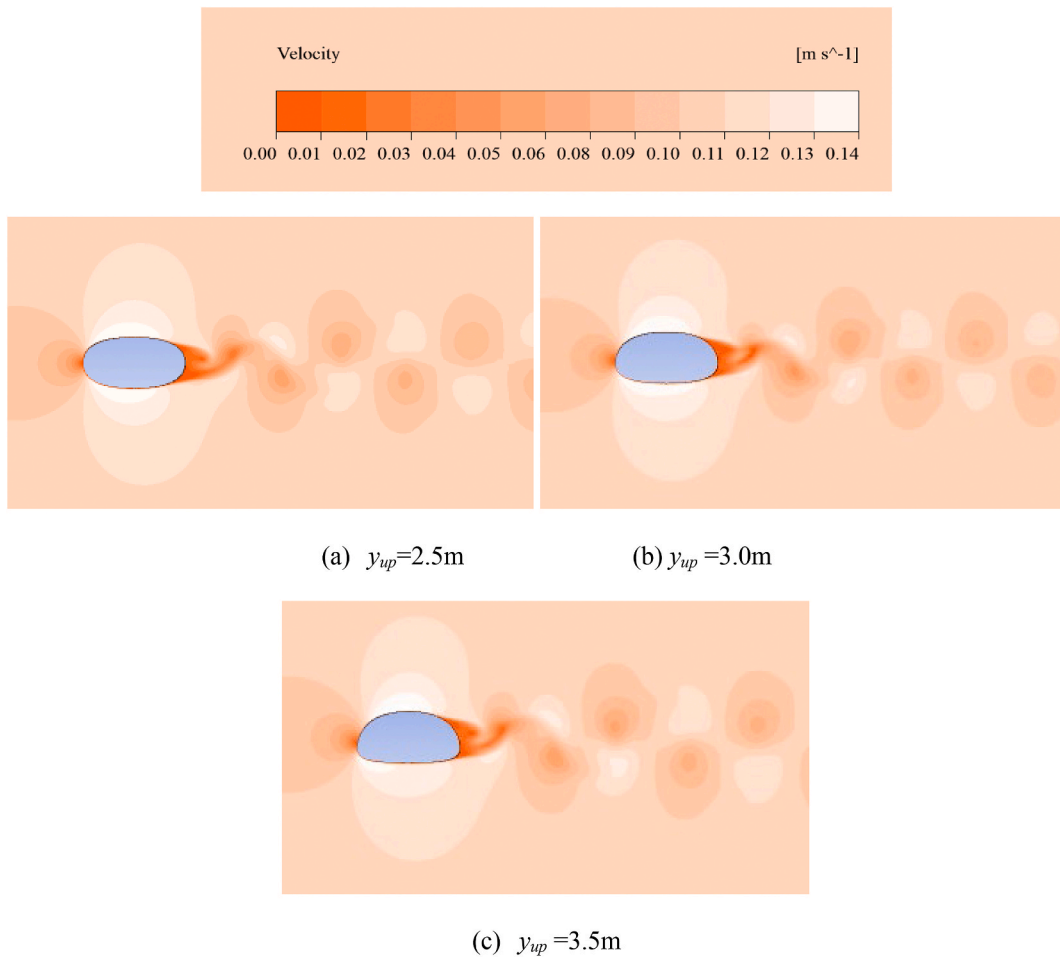


Fig. 7. Velocity magnitude contours for various  $y_{up}$ .

edge, implying the increase of  $C_l$  and  $C_d$ . With increasing  $r$ , the pressure difference between the upper and lower halves becomes smaller, which can explain the reduction in  $C_{l,rms}$  until reaching its lower limit around  $r = 2.5$  m (Fig. 9(a)). Lift can be generated by pressure difference between the upper and lower halves, and also the flow separation of the vortex shedding effect due to viscosity. For a symmetrical shape, the RMS lift is determined mainly by vortex shedding. The pressure difference between the upper and lower surfaces of the tunnel results in a minimum RMS lift around  $r = 2.5$  m. Hence, a slowly tapering tail with streamlined shape should be considered in the actual design. Furthermore, from Fig. 9(a), the boundary layer and pressure gradient can be basically categorized

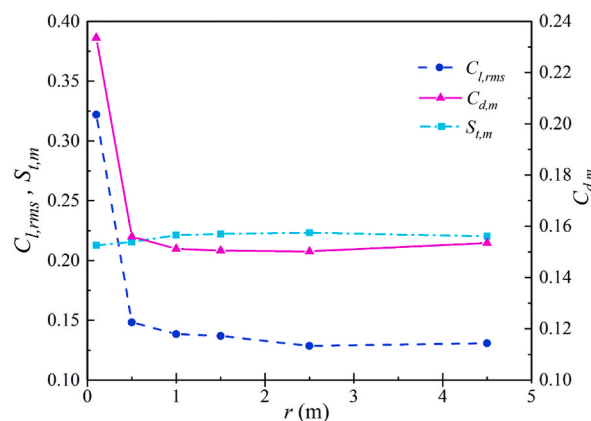
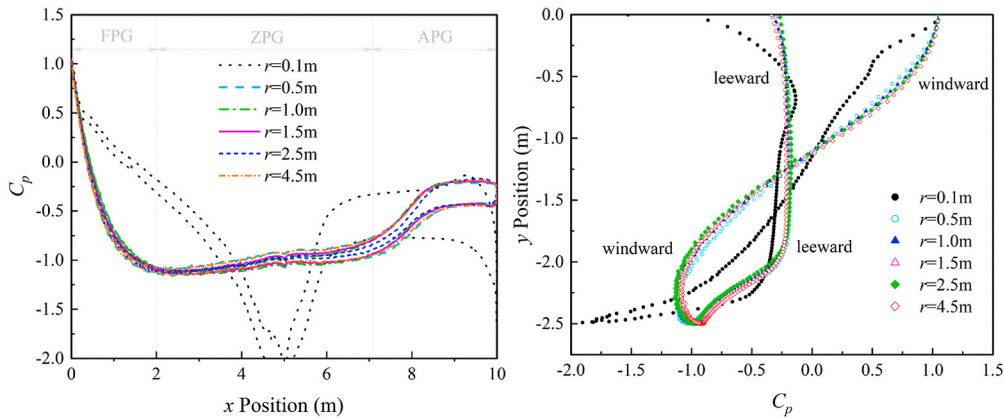


Fig. 8. Variation of dimensionless lift, drag, and Strouhal number with  $r$ .



(a)  $C_p$  of the cross-section upper and lower halves along x dir. (b)  $C_p$  of the cross-section lower half along y dir.

Fig. 9. Pressure distribution along cross section for various  $r$ . FPG: favorable pressure gradient; ZPG: zero-pressure gradient; APG: adverse pressure gradient.

into 3 regions: a favorable pressure gradient (FPG), a zero-pressure gradient (ZPG) and an adverse pressure gradient (APG), separated by two inflexion points near the leading and trailing edges due to the free stream flows along the side, separates from the leeward part, and induces comparatively large curvature near the windward and leeward inflexion locations.

For  $r \geq 0.5$  m, it is obvious from Fig. 9(b) that  $C_p$  shows a positive correlation with  $r$  near the leading edge, with an inverse distribution near the bottom, and the pressures at the leading edge and bottom part of the lower half vary only slightly; thus  $C_d$  shows little variation (Fig. 8). For  $r \geq 2.5$  m, the flow velocity increases as it passes around the leading edge of the tunnel cross section. The flow accelerates remarkably due to the large leading-edge stagnation region and the sharp change of flow direction, which causes a large pressure. Additionally, a bluffer tail with a flatter lower half shape develops causes a wider wake region near the trailing edge; both of these mechanisms cause the drag and RMS lift forces to increase.

#### 4.4. Effect of $b$

##### 4.4.1. Different $b$ for the upper and lower halves

Fig. 11 shows  $C_{l,rms}$ ,  $S_{l,m}$  and  $C_{d,m}$  for the cases  $b_{up} = 1.2$  m,  $r = 4.5$  m,  $y_{up} = 2.5$  m and  $b_{low} = 0.1$  m, 0.6 m, 1.2 m, 1.8 m, 2.4 m. Fig. 12 shows  $C_p$  of the upper and lower halves of the cross section as measured in the counterclockwise direction, when the shear stress vanishes and flow separation occurs on the lower half, and lift reaches its peak value.

It can be noted from Fig. 12(a), the absolute value of the negative pressure valley at the frontal part is larger than that at the leeward part. The FPG decreases (more negative) with increasing  $b_{low}$ . For  $b_{low} = 0.1$  m, the first local minimum is approximately located at  $x = 2$  m, and moves upstream with increasing  $b_{low}$  due to a blunter upstream corner on the lower half (Fig. 13). Similarly, the second local minimum is approximately at  $x = 7$  m, and moves downstream with increasing  $b_{low}$ . A plateau exists between these points. It is noted that the average pressure increases with increasing  $b_{low}$  due to the flatter profile of the lower half. The thickness of the boundary layer increases quickly and flow separation occurs in the APG region. At the end of the APG region, another plateau represents the leeward wake recirculation region, and the inflection point indicates flow separation. The lift force induced on a bluff body is mainly due to the pressure difference between its upper and lower halves, and the effect of vortex shedding. It can be deduced from Fig. 12 (a), comparing the pressure difference between upper and lower halves, that the minimal difference occurs when  $b$  values on both halves are the same. It can be concluded that a shape with the same  $b$  value shows the minimum pressure difference between the upper and lower halves. That is, it has the minimum  $C_l$ .

As for the drag force, it can be observed from Fig. 12 (b) that with different  $b_{low}$ , pressure coefficients of the leeward profile at the lower half keep approximately constant, but a difference becomes apparent on the windward half. In terms of the pressure distribution near the leading edge,  $C_p$  increases with increasing  $b_{low}$ , although the opposite occurs near the bottom. Consequently, the total pressure along the leading edge increases with  $b_{low}$ . Since the pressure distribution difference on the lower half of the leading edge between  $b_{low} = 0.1$  m and  $b_{low} = 0.6$  m is small, variation in  $C_d$  is not obvious. For  $b_{low} > 1.2$  m,  $C_d$  increases rapidly because  $C_p$  near the leading edge increases rapidly with increasing  $b_{low}$ .

The mechanism of the above phenomenon can be further interpreted as follows. The periodic vortex shedding in the wake region of the bluff body under oncoming uniform cross flow is known as the von Kármán vortex street [37,38]. Hydrodynamic and vortex street parameters show dependence on the cross section shape. The curvature of the upper and lower halves of the SFT cross section affects the interaction of the two separated boundary layers, and hence the vortex street generation process. For a symmetric shape, the vortex street propagates with a same magnitude of velocity and vorticity on the upper and lower halves, and the two separated shear layers coincide, approach, curve inwards and interact with each other more quickly, forming the von Kármán vortex street with a

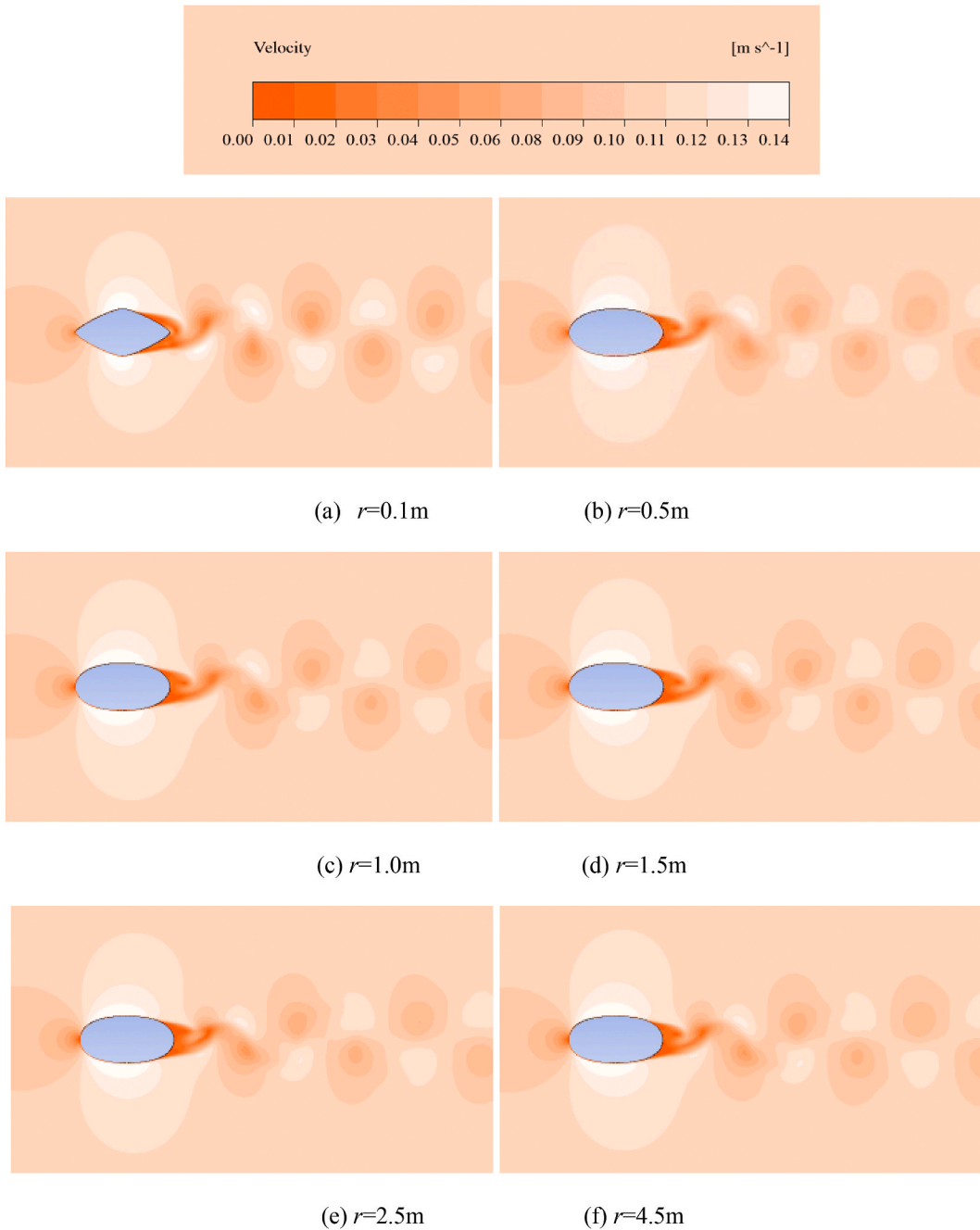


Fig. 10. Velocity magnitude contours for various  $r$ .

shorter vortex formation length at the trailing edge and resulting in a more rapid vortex shedding rate, and therefore, a larger  $S_b$ , smaller longitudinal vortex spacing  $l$  and  $C_l$  compared to the asymmetric cross sections.

#### 4.4.2. Same $b$ for the upper and lower halves

As a symmetrical tunnel profile is more favorable for minimizing lift but does not affect drag (section 4.4.1), the drag and lift coefficients for various  $b$  on both the upper and lower halves are discussed. Fig. 14 shows  $C_{l,rms}$ ,  $S_{t,m}$  and  $C_{d,m}$  for  $b_{up} = b_{low} = 0.1\text{ m}, 0.5\text{ m}, 1.2\text{ m}, 1.8\text{ m}, 2.4\text{ m}, r = 4.5\text{ m}$ , and  $y_{up} = 2.5\text{ m}$ . Fig. 16 shows the velocity magnitude contours. In order to describe the  $C_{l,rms}$  tendency clearly, here  $C_p$  curves for only three tunnel profiles are shown. Fig. 15(a) shows that the pressure difference between upper and lower halves increases with increasing  $b$ , thus  $C_{l,rms}$  increases. It is clear that the pressure difference between the windward surface and leeward region reflects the magnitude of drag. From Fig. 15 (b), pressure coefficients on the leeward lower part are similarly

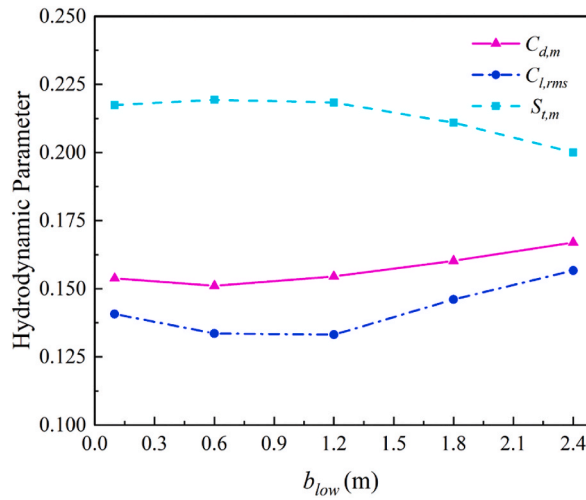
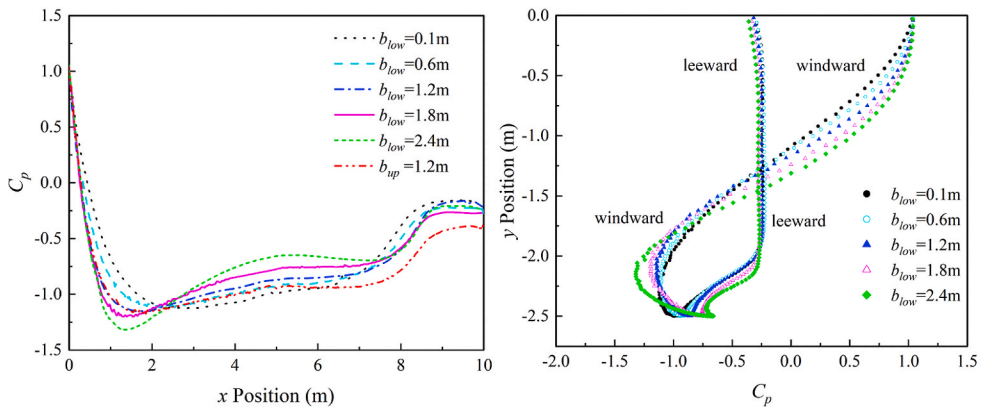


Fig. 11. Variation of dimensionless lift, drag, and Strouhal number with  $b_{low}$ .



(a)  $C_p$  of the cross-section lower and upper halves along x dir. (b)  $C_p$  of the cross-section lower half along y dir.

Fig. 12. Pressure distribution along cross section for various  $b_{low}$ .

consistent, but  $C_p$  increases gradually with increasing  $b$  near the front of the leading edge. This occurs despite the fact that in a localized region near the bottom of the leading edge  $C_p$  becomes more negative with increasing  $b$ . That is,  $C_d$  increases as  $b$  increases.

It should be noted that increasing  $b$  or  $r$  of the parametric Bézier curve doesn't always act to make the body bluffer for a fixed aspect ratio. The combined effect of  $b$  and  $r$  affect drag and lift, making optimal profile selection complicated. Nevertheless, from section 4.4.1,  $C_d$  and  $C_{l,rms}$  are not always independent. The optimal cross section design should be considered in the arrangement, inclined angle, and stiffness of the mooring system and the buoyancy control of the SFT.

## 5. Optimization algorithms

### 5.1. Multi-objective optimization

A multi-objective problem compromises a vector of decision variables satisfying a number of inequality or equality constraints to give optimal solutions to all objectives simultaneously [39]. In this study, since it is unrealistic to solve all the possible SFT cross-section shapes with a combination of different variables using the complicated and time-consuming CFD code, and with the problems of the interdependent distributions of  $C_{l,rms}$  and  $C_{d,m}$ , we consider  $C_{l,rms}$  and  $C_{d,m}$  as two minimization objectives and a function of four Bézier curve parameters varying independently, using an artificial intelligence (AI) optimization algorithm. Concerning the BP parameter constraint conditions in section 2.1, the problem can be described as follows:

Optimization parameters:  $y_{up}$ ,  $r$ ,  $b_{up}$ ,  $b_{low}$

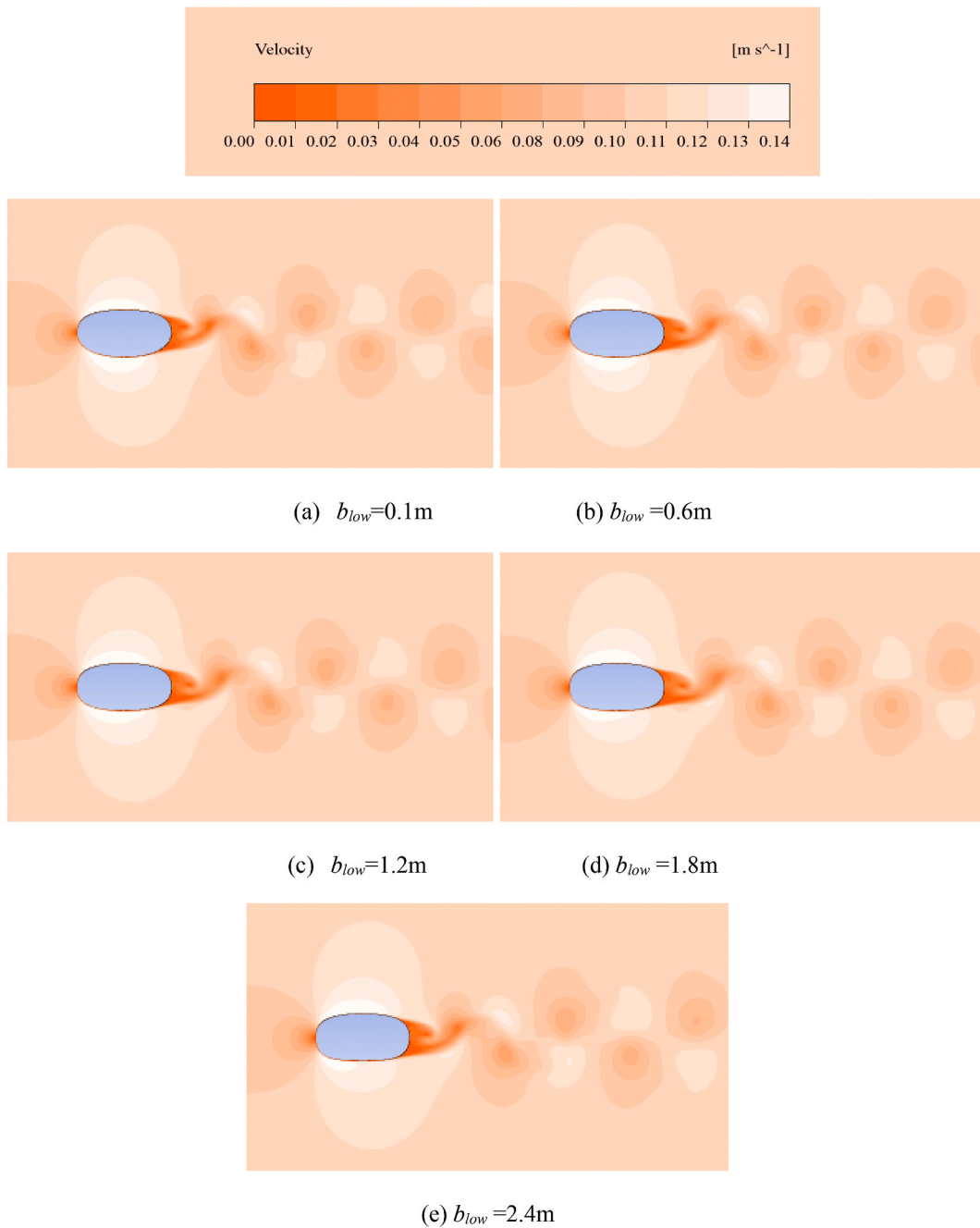


Fig. 13. Velocity magnitude contours for various  $b_{low}$ .

$$\text{Optimization objectives: } \begin{cases} \min. C_{l,rms}(y_{up}, r, b_{up}, b_{low}) \\ \min. C_{d,m}(y_{up}, r, b_{up}, b_{low}) \end{cases}$$

$$\text{Constraint conditions: } \begin{cases} 0 \leq y_{up} \leq 5 \\ 0 < r \leq 2.5 \\ 0 < b_{up} < \min.(y_{up}, \sqrt{10r/3}) \\ 0 < b_{low} < \min.(5 - y_{up}, \sqrt{10r/3}) \end{cases}$$

### 5.2. Hybrid neural networks and genetic algorithm

A NN [40,41] with multiple layers was applied to predict the hydrodynamic properties under various possible BP curve parameters.

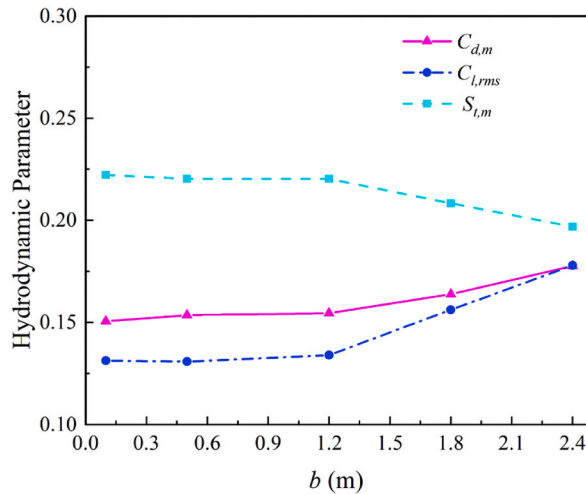
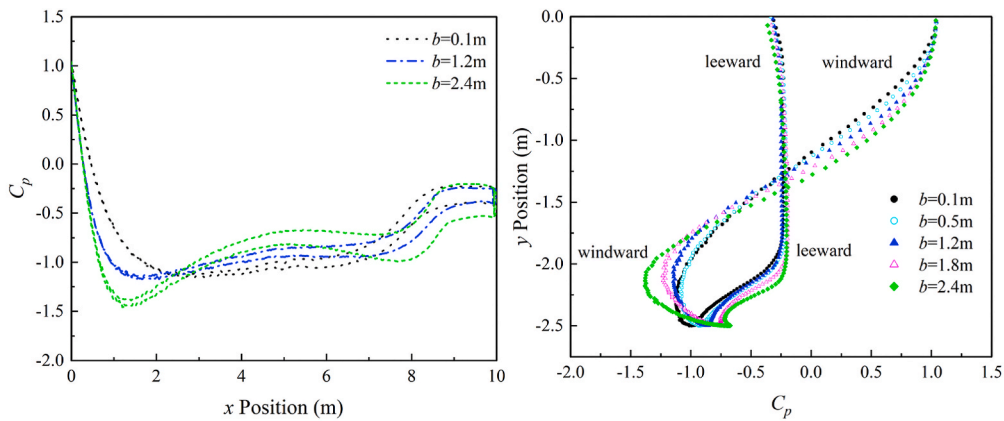


Fig. 14. Variation of dimensionless lift, drag, and Strouhal number with  $b$ .



(a)  $C_p$  of the cross-section upper and lower halves along x dir. (b)  $C_p$  of the cross-section lower half along y dir.

Fig. 15. Pressure distribution along cross section for various  $b$ .

NN's have superior capacity in forecasting the relationships between input and output variables for data-driven prediction. The backpropagation (BP) learning algorithm is the most popular NN training method and is well suited for unseen features such as learning from previous experience samples [42]. Hence, it is unnecessary to simulate all the possible tunnel cross-section shapes a priori, with the ability of NN's to recognize arbitrary profile features.

In this study, a GA [43] was used to optimize the initial weights and thresholds of the BP algorithm, which is a weight optimization architecture commonly called "GA-BP". With the ability to produce robust and effective results for noisy and discontinuous data, GA can search the entire solution space to find the global optimum via selection, crossover and mutation processes, to avert convergence problems from getting stuck in local minima [44].

In this study, a three-layer BP NN structure was applied as a prediction and optimization model. Four neurons were contained in the input layer, denoting  $y_{up}$ ,  $r$ ,  $b_{up}$ , and  $b_{low}$  to determine the tunnel cross-section shape. All these parameters of every case were randomly generated within the constraints and normalized into the range of  $(-1,1)$ . The hidden layer consisted of 10 neurons with the "tansig" transfer function [45]. Two neurons with linear transfer functions were applied as the output layer, denoting  $C_{l,rms}$  and  $C_{d,m}$ . Therefore, a "4-10-2" BP-GA structure was employed in this study. The detailed parameters of the hybrid BP-GA structure are shown in Table 3.

The BP algorithm optimizes weights and thresholds to minimize prediction error to the training data set, while the GA prevents the BP solution from getting stuck in local minima of the error. To verify the effectiveness of the BP-GA optimization process, further analysis and discussion are conducted in section 5.3.

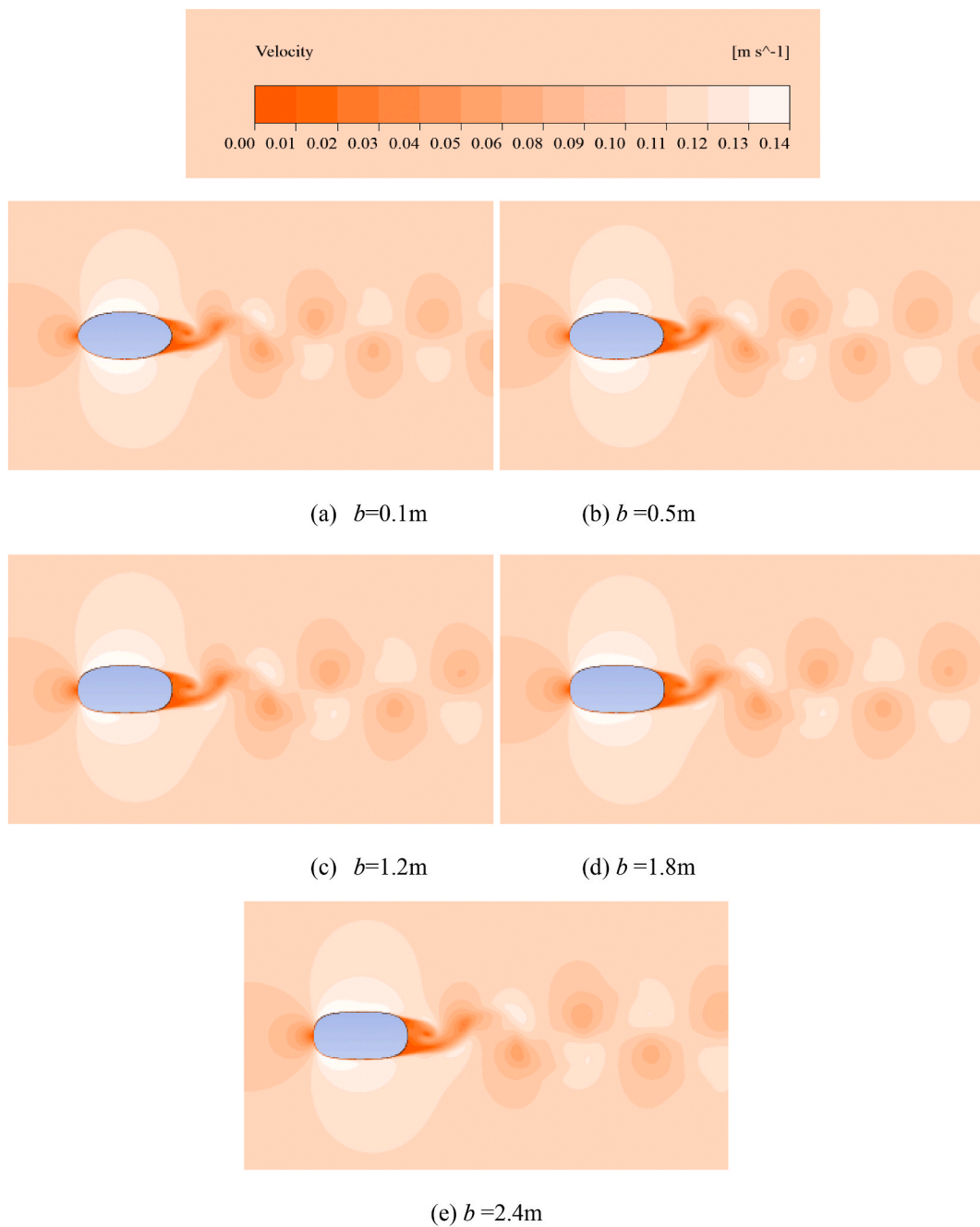


**Fig. 16.** Velocity magnitude contours for various  $b$ .

**Table 3**  
Input parameters used in the hybrid BP-GA model.

| Input parameters             | The BP-GA Model |
|------------------------------|-----------------|
| Training times               | 500             |
| Total squared error          | 0.0001          |
| Learning rate                | 0.01            |
| Population size              | 50              |
| Max. generations             | 100             |
| Crossover probability        | 0.9             |
| Uniform mutation probability | 0.01            |

### 5.3. Results analysis and verification

Fig. 17 illustrates the optimal cross-section selection process by using hybrid BP-GA including three main steps: establish the initial population model including training and testing data sets; determine the BP training set by applying the GA optimization; and conduct the BP prediction process and verify with CFD analysis.

**Step 1.** Two procedures are included in this step: first, randomly generate  $n = 60$  groups of Bézier curve parameters within the constraints and obtain  $C_{l,rms}$  and  $C_{d,m}$  as objective functions by conducting reliable CFD simulations. Note that the randomly generated parameters should be uniformly and reasonably distributed within the constraints to increase the accuracy and reliability of further optimization; second, randomly select  $m = 50$  groups of samples as a training set and the remaining 10 samples as a testing set to execute the BP training process.

**Step 2.** The GA implemented by a roulette-wheel algorithm is applied to the thresholds and weights optimization of the BP NN structure. The target of this optimization is to maximize the fitness value to achieve ideal prediction results. The mathematical relationship between the input parameters comprised of 4 Bézier curve variables and output objectives including  $C_{l,rms}$ , and  $C_{d,m}$  is established after the training process of the hybrid BP-GA. After comparing the prediction results with the testing set, the Average Root Mean Square Error (ARMSE) which is a measure of scatter or lack of precision, and Square Pearson Coefficient  $R^2$  of each case are calculated as two discriminant criteria. Here, the ARMSE and  $R^2$  are expressed by Eqs. (12) and (13)

$$ARMSE = \sqrt{\frac{1}{10} \sum_{i=1}^{10} (y_p - y_c)_i^2} \tag{12}$$

$$R^2 = \frac{\sum_{i=1}^{10} [(y_{p,i} - y_{p,m}) \times (y_{c,i} - y_{c,m})]^2}{\sum_{i=1}^{10} [(y_{p,i} - y_{p,m})^2] \times \sum_{i=1}^{10} [(y_{c,i} - y_{c,m})^2]} \tag{13}$$

where  $y_p$  and  $y_c$  represent for the predicted and calculated values of  $C_{l,rms}$  or  $C_{d,m}$ , respectively. The subscript  $m$  represents the mean value.

To ensure the representativeness of the training set, the ARMSE is restricted to a maximum training error  $\epsilon$ , here taken as 0.01, and an  $R^2 > 0.8$ , which signifies a satisfactory performance [46]. A statistical comparison of the mean drag and RMS lift coefficients between the BP-GA training results (the predicted values) and the testing set (the CFD results) is performed in Fig. 18. It clearly shows the max. ARMSE = 0.009 with  $R^2 = 0.861$  for  $C_{d,m}$ , and 0.010 with  $R^2 = 0.822$  for  $C_{l,rms}$ , suggesting a qualitatively good performance of the hybrid BP-GA training process.

**Step 3.** After determining the training set to use in the optimal cross-section prediction,  $C_{l,rms}$  and  $C_{d,m}$  of randomly cases comprised of Bézier curve parameters within constrains are predicted with the utilization of the trained hybrid BP-GA NN. The prediction process is terminated by searching for  $C_{l,rms}$  and  $C_{d,m}$  values smaller than the minimum sample results in the training and testing sets. The output optimal SFT cross-section Bezier parameters are then validated with CFD.

Fig. 19 shows minimum values of  $C_{l,rms}$ , and  $C_{d,m}$  among the 60 original samples, the predicted values for the optimized cross section as output the by BP-GA, and the actual values output by CFD of the optimal cross section. The Bézier curve parameters of the optimal SFT cross section are:  $b_{up} = b_{low} = 1$  m;  $r = 3$  m;  $y_{up} = y_{low} = 2.5$  m. The forecast has an error of 1.7% compared with the CFD validation result, which illustrates the feasibility and reliability of the hybrid BP-GA prediction. The optimized SFT cross section  $C_{d,m}$  is 0.9% lower, and  $C_{l,rms}$  is 6.3% lower, than the mean drag and the RMS lift coefficients of the original 60 random samples. In this case, the minimum mean drag value of the sample is small, so the reduction of the optimal value is not obvious. However, it also shows that the sample is representative which the approximate optimal solution has already been covered. Overall, an optimized profile with better hydrodynamic performance than the original 60 samples is achieved by the hybrid BP-GA optimization.

## 6. Conclusions

To overcome a lack of research on hydrodynamic performance of SFT cross sections, a parametric Bézier curve is applied to SFT cross section geometry design, and a sensitivity analysis to the Bézier curve parameters is carried out. The RMS lift and mean drag coefficients are considered as objective functions and are optimized by a hybrid BP-GA structure. The main conclusions are briefly summarized as follows:

- The Bézier curve parameters analysis shows  $y_{up}$  with a value of half of the total tunnel height achieves the minimum RMS  $C_l$  and mean  $C_d$ . To reduce the RMS lift force, a symmetrical shape with same  $b$  on both upper and lower surfaces should be used. The pressure difference between the leading edge and trailing edge reflects the magnitude of drag. For a SFT cross section with a fixed and relatively thick aspect ratio, a better hydrodynamic performance can't be achieved by continuously minimizing the leading edge radius, because a sharp leading edge and apex shape causes flow detachment.

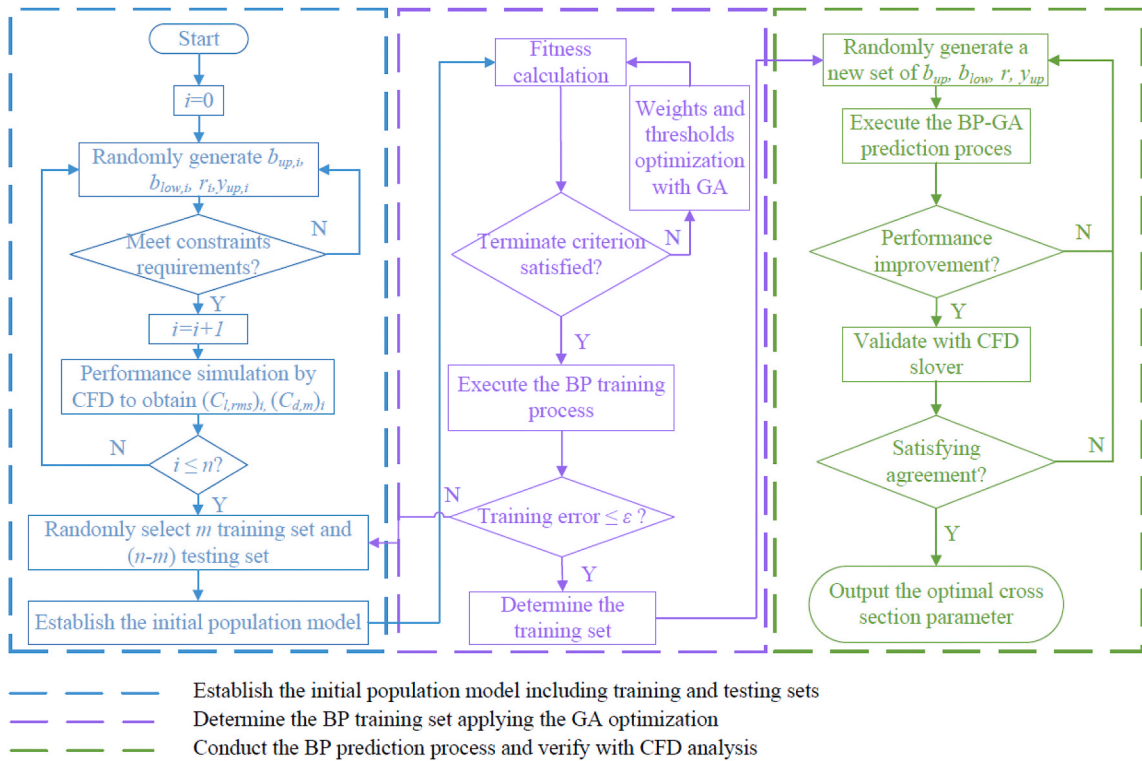


Fig. 17. Flow chart of the hybrid BP-GA optimization process.

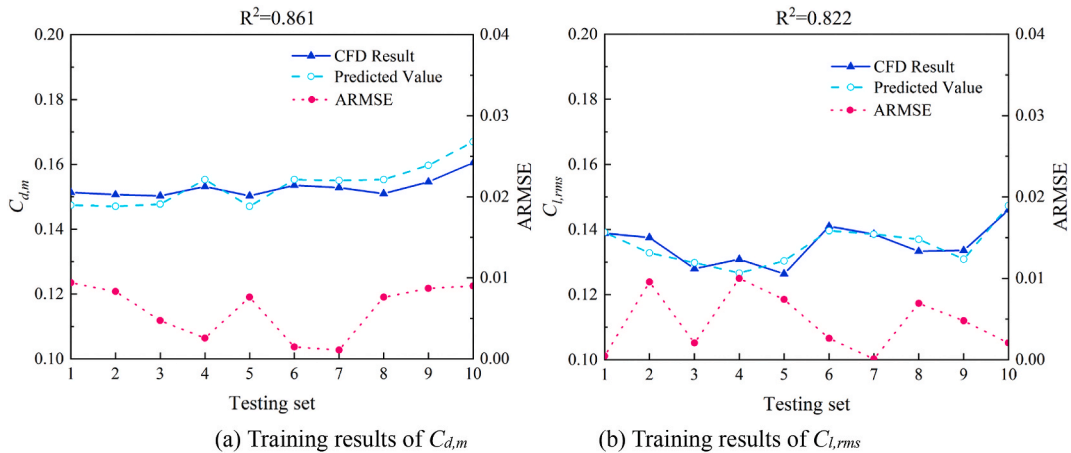


Fig. 18. Comparison of the BP-GA training results with 10 testing samples.

- The numerical CFD simulation are verified with a theoretical method to determine the drag and lift by employing the Kármán vortex street parameters, despite limitations due to basic assumptions.
- A neural network with a backpropagation learning algorithm benefits from combination with a GA. This reduces the need for time-consuming CFD analyses, and increases the accuracy, reliability and goodness of prediction of the SFT cross section design. Therefore, hybrid BP-GA is an effective tool to optimize the complex interdependency of Bézier curve parameters.

In spite of these achievements of the Bézier curve parameter analysis and applicability of the hybrid BP-GA method, some restrictions and future work still should be noted in this study:

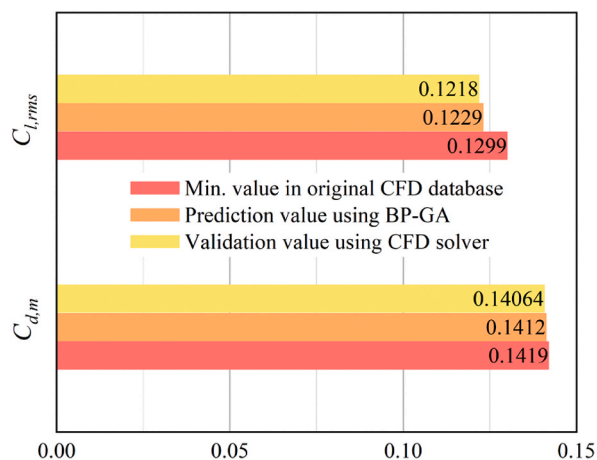


Fig. 19. Hydrodynamic performance comparison after optimization.

- A fixed aspect ratio for the SFT cross section is used. It is worth noting that the drag and lift of each Bézier curve parameter combination will be different for different aspect ratios. However, the basic methodology of CFD simulation combined with the hybrid BP-GA optimization process is still applicable.
- The future work should consist of a larger training set to optimize the algorithm variables and increase forecasting robustness and accuracy.

#### Declaration of competing interest

The authors declare that they have no known competing financial interests or personal relationships that could have appeared to influence the work reported in this paper.

#### Acknowledgement

The study presented in this paper was conducted in the submerged floating tunnel research project funded by China Communications Construction Company Ltd. (CCCC) and jointly carried out by universities, scientific research institutes, engineering consulting firms, design and construction companies in China and the Netherlands. The authors would like to acknowledge C.J. (Carlos) Simão Ferreira for his contribution in elucidating the knowledge of airfoil design.

#### References

- [1] Ahrens D. Submerged floating tunnels - a concept whose time has arrived. *Tunn Undergr Space Technol* 1997. [https://doi.org/10.1016/s0886-7798\(97\)90022-5](https://doi.org/10.1016/s0886-7798(97)90022-5).
- [2] Lin H, Xiang Y, Yang Y. Vehicle-tunnel coupled vibration analysis of submerged floating tunnel due to tether parametric excitation. *Mar Struct* 2019. <https://doi.org/10.1016/j.marstruc.2019.102646>.
- [3] Li K, Jiang X. Research on section form of submerged floating tunnels considering structural internal force optimization under fluid action. In: *procedia engineering*. <https://2016.doi.org/10.1016/j.proeng.2016.11.551>.
- [4] Crighton DG. The Kutta condition in unsteady flow. *Annu Rev Fluid Mech* 1985. <https://doi.org/10.1146/annurev.fl.17.010185.002211>.
- [5] Li Q, Jiang S, Chen X. Experiment on pressure characteristics of submerged floating tunnel with different section types under wave condition. *Pol Marit Res* 2018. <https://doi.org/10.2478/pomr-2018-0112>.
- [6] Gang L, Xiao-jun Z, Jian-xun C. The dynamic response of an experimental floating tunnel with different cross sections under explosive impact. *J Coast Res* 2018. <https://doi.org/10.2112/si82-031.1>.
- [7] <https://www.lstc.com/products/lstc-dyna>.
- [8] Hajabdollahi F, Rafsanjani HH, Hajabdollahi Z, Hamidi Y. Multi-objective optimization of pin fin to determine the optimal fin geometry using genetic algorithm. *Appl Math Model* 2012. <https://doi.org/10.1016/j.apm.2011.05.048>.
- [9] Basumatary M, Biswas A, Misra RD. CFD analysis of an innovative combined lift and drag (CLD) based modified Savonius water turbine. *Energy Convers Manag* 2018. <https://doi.org/10.1016/j.enconman.2018.08.025>.
- [10] Wang X, Lu Y. Optimization of the cross section area on the meridian surface of the 1400-MW canned nuclear coolant pump based on a new medial axial transform design method. *Ann Nucl Energy* 2018. <https://doi.org/10.1016/j.anucene.2018.01.027>.
- [11] Lee JJ, Jung UJ, Park GJ. Shape optimization of the workpiece in the forging process using equivalent static loads. *Finite Elem Anal Des* 2013. <https://doi.org/10.1016/j.finel.2013.01.005>.
- [12] Garg N, Pearce BW, Brandner PA, Phillips AW, Martins JRRA, Young YL. Experimental investigation of a hydrofoil designed via hydrostructural optimization. *J Fluid Struct* 2019. <https://doi.org/10.1016/j.jfluidstructs.2018.10.010>.
- [13] Bézier P. Mathematical and practical possibilities OF UNISURF. In: *Computer aided geometric design.*; 1974. <https://doi.org/10.1016/b978-0-12-079050-0.50012-6>.
- [14] Wang A, Zhao G, Hou F. Constructing Bézier curves with monotone curvature. *J Comput Appl Math* 2019. <https://doi.org/10.1016/j.cam.2019.01.004>.
- [15] <https://www.ansys.com>.
- [16] Jung S, Choi W, Martins-Filho LS, Madeira F. An implementation of self-organizing maps for airfoil design exploration via multi-objective optimization technique. *J Aero Technol Manag* 2016. <https://doi.org/10.5028/jatm.v8i2.585>.

- [17] Nikolaev NV. Optimization of airfoils along high-aspect-ratio wing of long-endurance aircraft in trimmed flight. *J Aero Eng* 2019. [https://doi:10.1061/\(ASCE\)AS.1943-5525.0001086](https://doi:10.1061/(ASCE)AS.1943-5525.0001086).
- [18] Derksen RW, Rogalsky T. Bezier-PARSEC: an optimized aerofoil parameterization for design. *Adv Eng Software* 2010. <https://doi:10.1016/j.advengsoft.2010.05.002>.
- [19] Rogalsky TP. *Acceleration of differential evolution for aerodynamic design*. 2004.
- [20] Tveit P. Ideas on downward arched and other underwater concrete tunnels. *Tunn Undergr Sp Technol*; 2000. [https://doi:10.1016/S0886-7798\(00\)00031-6](https://doi:10.1016/S0886-7798(00)00031-6).
- [21] Larssen RM, Jakobsen SE. Submerged floating tunnels for crossing of wide and deep fjords. In: *Procedia engineering*; 2010. <https://doi:10.1016/j.proeng.2010.08.020>.
- [22] Muhammad N, Ullah Z, Choi DH. Performance evaluation of submerged floating tunnel subjected to hydrodynamic and seismic excitations. *Appl Sci* 2017. <https://doi:10.3390/app7111122>.
- [23] American Association of State Highway, Officials T. *A policy on geometric design of highways and streets*. 2018.
- [24] JTG/T D70 Ministry of transport of the people's Republic of China, *guidelines for design of highway tunnel*. 2010 [in Chinese].
- [25] Kuzmin D, Mierka O, Turek S. On the implementation of the fr-turbulence model in incompressible flow solvers based on a finite element discretisation. *Int J Comput Sci Math* 2007. <https://doi:10.1504/ijcsm.2007.016531>.
- [26] Catalano P, Wang M, Iaccarino G, Moin P. Numerical simulation of the flow around a circular cylinder at high Reynolds numbers. *Int J Heat Fluid Flow* 2003. [https://doi:10.1016/S0142-727X\(03\)00061-4](https://doi:10.1016/S0142-727X(03)00061-4).
- [27] Van Doormaal JP, Raithby GD. Enhancements of the simple method for predicting incompressible fluid flows. *Numer Heat Tran* 1984. <https://doi:10.1080/01495728408961817>.
- [28] Zhang J, Wu W, Hu J. A numerical study of the effects of the longitudinal baffle on nickel ore slurry sloshing in a prismatic cargo hold. *Mar Struct* 2016. <https://doi:10.1016/j.marstruc.2016.01.003>.
- [29] Ansys Inc. *ANSYS fluent UDF manual*. Knowl Creat Diffus Util 2013.
- [30] <https://www.pipeflow.com/pipe-pressure-drop-calculations/pipe-roughness>.
- [31] Ong MC, Utnes T, Holmedal LE, Myrhaug D, Pettersen B. Numerical simulation of flow around a smooth circular cylinder at very high Reynolds numbers. *Mar Struct* 2009. <https://doi:10.1016/j.marstruc.2008.09.001>.
- [32] Lin YH, Lu PY, Lin CW. Numerical simulation of maximum wave loads and run-up heights on offshore wind turbine foundations influenced by the instability of bichromatic wave groups. *Mar Struct* 2019. <https://doi:10.1016/j.marstruc.2019.102648>.
- [33] James WD, Paris SW, Malcolm GN. Study of viscous crossflow effects on circular cylinders at high Reynolds numbers. *AIAA J* 1980. <https://doi:10.2514/3.50855>.
- [34] Sallet DW. Lift force due to VON KARMAN'S vortex wake. *J Hydraulics* 1973. <https://doi:10.2514/3.62951>.
- [35] Attanapola. *Dhanushi nayanatara. Numerical simulation of viscous shear flow around tandem cylinders*. MS thesis. NTNU; 2018.
- [36] Pelletier A, Mueller TJ. Low Reynolds number aerodynamics of low-aspect-ratio, thin/flat/cambered-plate wings. *J Aircraft* 2000. <https://doi:10.2514/2.2676>.
- [37] Kármán TV. On the mechanism of the drag a moving body experiences in a fluid. *Prog Aero Sci* 2013. <https://doi:10.1016/j.paerosci.2013.03.004>.
- [38] Abrahamsen Prsic M, Ong MC, Pettersen B, Myrhaug D. Large Eddy Simulations of flow around a circular cylinder close to a flat seabed. *Mar Struct* 2016. <https://doi:10.1016/j.marstruc.2016.01.002>.
- [39] Demirkaya G, Besarati S, Vasquez Padilla R, et al. Multi-objective optimization of a combined power and cooling cycle for low-grade and midgrade heat sources. *J Energy Resour Technol* 2012. <https://doi:10.1115/1.4005922>.
- [40] Ahn Y, Kim Y, Kim SY. Database of model-scale sloshing experiment for LNG tank and application of artificial neural network for sloshing load prediction. *Mar Struct* 2019. <https://doi:10.1016/j.marstruc.2019.03.005>.
- [41] Li CB, Choung J, Noh MH. Wide-banded fatigue damage evaluation of Catenary mooring lines using various Artificial Neural Networks models. *Mar Struct* 2018. <https://doi:10.1016/j.marstruc.2018.03.013>.
- [42] Papadrakakis M, Lagaros ND, Tsompanakis Y. Structural optimization using evolution strategies and neural networks. *Comput Methods Appl Mech Eng* 1998. [https://doi:10.1016/S0045-7825\(97\)00215-6](https://doi:10.1016/S0045-7825(97)00215-6).
- [43] Silva RF da, Teófilo FAF, Parente E, Melo AMC de, Holanda AS de. Optimization of composite catenary risers. *Mar Struct* 2013. <https://doi:10.1016/j.marstruc.2013.04.002>.
- [44] Yan C, Li M, Liu W, Qi M. Improved adaptive genetic algorithm for the vehicle insurance fraud identification model based on a BP neural network. *Theor Comput Sci* 2019. <https://doi:10.1016/j.tcs.2019.06.025>.
- [45] Vogl TP, Mangis JK, Rigler AK, Zink WT, Alkon DL. Accelerating the convergence of the back-propagation method. *Biol Cybern* 1988. <https://doi:10.1007/BF00332914>.
- [46] Coulibaly P, Baldwin CK. Nonstationary hydrological time series forecasting using nonlinear dynamic methods. *J Hydrol* 2005. <https://doi:10.1016/j.jhydrol.2004.10.008>.

## APPENDIX NOTATION

$b_{low}$  =:  $b$  at lower half of the tunnel profile  
 $b_{up}$  =:  $b$  at upper half of the tunnel profile  
 $C_d$  =: Drag coefficient  
 $C_{d,m}$  =: Mean drag coefficient  
 $C_l$  =: Lift coefficient  
 $C_{l,max}$  =: Max. lift coefficient  
 $C_{l,rms}$  =: RMS lift coefficient variability  
 $C_p$  =: Pressure coefficient  
 $F_{l,d}$  =: Lift or drag force per meter  
 $G_b$  =: Generation of  $k$  due to buoyancy  
 $G_k$  =: Generation of  $k$  due to the mean velocity gradients  
 $H$  =: Vertical clearance of tunnel cross section  
 $h$  =: Lateral consecutive vortex spacing  
 $i$  =: Slope  
 $k$  =: Turbulence kinetic energy  
 $l$  =: Longitudinal consecutive vortex spacing  
 $p$  =: Pressure  
 $p_{ref}$  =: Reference pressure  
 $R$  =: Curb or sidewalk  
 $r$  =: Leading edge radius  
 $Re$  =: Reynolds number  
 $S_k, S_\epsilon$  =: User-defined source terms  
 $S_{max}$  =: Grid size at outer boundaries  
 $S_{min}$  =: Grid size of the tunnel profile  
 $S_t$  =: Strouhal number

$t$  =: Time  
 $U$  =: Uniform flow velocity  
 $W$  =: Width clearance of tunnel cross section  
 $Y^+$  =: Dimensionless wall distance  
 $y_{low}$  =:  $y$  at lower half of the tunnel profile  
 $Y_M$  =: Contribution of the fluctuating dilatation in compressible turbulence to the overall dissipation rate  
 $y_{up}$  =:  $y$  at upper half of the tunnel profile  
 $\alpha_k$  =: Inverse effective Prandtl numbers for  $k$   
 $\alpha_\varepsilon$  =: Inverse effective Prandtl numbers for  $\varepsilon$   
 $\varepsilon$  =: Turbulence dissipation rate  
 $\mu$  =: Fluid dynamic viscosity  
 $\mu_{eff}$  =: Effective viscosity  
 $\rho$  =: Fluid density